AGU PUBLICATIONS

JGR

Journal of Geophysical Research: Solid Earth

RESEARCH ARTICLE

10.1002/2017JB014973

Key Points:
- Reaction of pyrite to pyrrhotite induced by seismic frictional heating confined to three slip zones in prism sediments from the Japan Trench
- Maximum temperature experienced by the three fault zones is constrained to 640–800°C
- Mineral magnetic identification of trace amounts of pyrrhotite enables tracing seismic slip in pyrite-bearing sediments

Supporting Information:
- Supporting Information S1
- Table S1

Correspondence to:
T. Yang,
yangtao@cug.edu.cn;
t.yang@uu.nl

Citation:
Yang, T., Dekkers, M. J., & Chen, J. (2018). Thermal alteration of pyrite to pyrrhotite during earthquakes: New evidence of seismic slip in the rock record. *Journal of Geophysical Research: Solid Earth*, *123*, 1116–1131. https://doi.org/10.1002/2017JB014973

Received 11 SEP 2017
Accepted 4 FEB 2018
Accepted article online 13 FEB 2018
Published online 26 FEB 2018

Thermal Alteration of Pyrite to Pyrrhotite During Earthquakes: New Evidence of Seismic Slip in the Rock Record

Tao Yang[1,2,3], Mark J. Dekkers[3], and Jianye Chen[4]

[1]Hubei Subsurface Multi-Scale Imaging Key Laboratory, Institute of Geophysics and Geomatics, China University of Geosciences, Wuhan, China, [2]Key Laboratory of Seismic Observation and Geophysical Imaging, Institute of Geophysics, China Earthquake Administration, Beijing, China, [3]Paleomagnetic Laboratory Fort Hoofddijk, Department of Earth Sciences, Utrecht University, Utrecht, Netherlands, [4]HPT Laboratory, Department of Earth Sciences, Utrecht University, Utrecht, Netherlands

Abstract Seismic slip zones convey important information on earthquake energy dissipation and rupture processes. However, geological records of earthquakes along exhumed faults remain scarce. They can be traced with a variety of methods that establish the frictional heating of seismic slip, although each has certain assets and disadvantages. Here we describe a mineral magnetic method to identify seismic slip along with its peak temperature through examination of magnetic mineral assemblages within a fault zone in deep-sea sediments cored from the Japan Trench—one of the seismically most active regions around Japan—during the Integrated Ocean Drilling Program Expedition 343, the Japan Trench Fast Drilling Project. Fault zone sediments and adjacent host sediments were analyzed mineral magnetically, supplemented by scanning electron microscope observations with associated energy dispersive X-ray spectroscopy analyses. The presence of the magnetic mineral pyrrhotite appears to be restricted to three fault zones occurring at ~697, ~720, and ~801 m below sea floor in the frontal prism sediments, while it is absent in the adjacent host sediments. Elevated temperatures and coseismic hot fluids as a consequence of frictional heating during earthquake rupture induced partial reaction of preexisting pyrite to pyrrhotite. The presence of pyrrhotite in combination with pyrite-to-pyrrhotite reaction kinetics constrains the peak temperature to between 640 and 800°C. The integrated mineral-magnetic, microscopic, and kinetic approach adopted here is a useful tool to identify seismic slip along faults without frictional melt and establish the associated maximum temperature.

1. Introduction

The 2011 Mw 9.0 Tohoku-oki earthquake off the northeast coast of Honshu Island (Japan; Figure 1a) produced a huge coseismic displacement (~50 m) reaching the sea floor at the trench axis of the Japan Trench. It caused an unprecedentedly devastating tsunami in northeastern Japan (e.g., Simons et al., 2011). To understand the mechanism of such unusual huge slip near a trench, the Integrated Ocean Drilling Program (IODP) Expedition 343, the Japan Trench Fast Drilling Project (JFAST), penetrated the plate-boundary fault in the region where large shallow slip occurred during the earthquake (Figure 1a) (Chester, Mori, et al., 2013). An area-balanced palinspastic reconstruction based on the borehole geophysical measurements and core observations revealed that the cumulative displacement across the plate boundary at the drill site (IODP Site C0019) is at least ~3.2 km (Chester, Rowe, et al., 2013). The 50 m coseismic slip of the 2011 event is estimated to account at most for only about half of the plate motion since the Common Era 869 Jogan earthquake (Scholz, 2014). Therefore, previous great earthquakes recurring episodically with an interval of ~500 to ~1,000 years (Sawai et al., 2015) should have caused significant additional shallow coseismic slip propagating through the cored accretionary wedge. Investigation of those historical earthquakes would thus shed light on understanding the subduction history of the incoming Pacific Plate. To this end, an overall picture of the fault zones is required.

Many earthquake fault zone studies, however, share a common denominator: it is difficult to find geological records of seismic fault slip and to locate seismic slip zones in the rock record (Han et al., 2007). Two common approaches have been proposed to identify previous earthquake records: one is based on the analysis of structures produced by seismic processes and the second approach involves establishing the frictional heating of seismic slip (Rowe & Griffith, 2015).

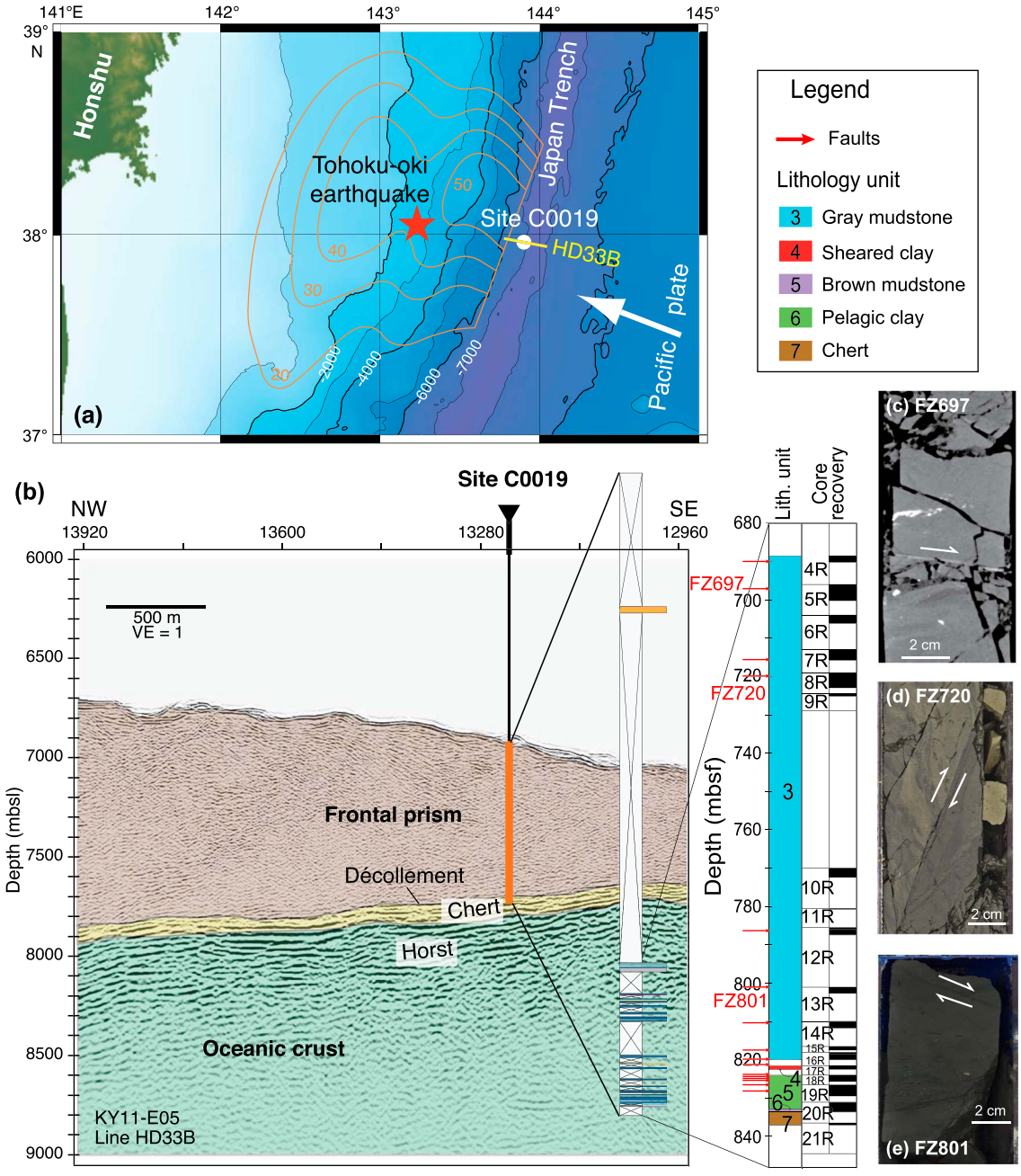

Figure 1. (a) Map of part of the Japan Trench showing location of Site C0019 with white filled circle. The red star indicates the epicenter of the 2011 Mw 9.0 Tohoku-Oki earthquake. Contours of slip during the earthquake rupture are taken from Yue and Lay (2011). The white arrow indicates the plate convergence vector (Argus et al., 2011). (b) Interpreted seismic profile along Line HD33B (indicated in Figure 1a) showing the site location cored during IODP Expedition 343. Inset shows the lithology and recovery at cored interval of Hole C0019E (688.50–836.81 m bsf). The dark parts indicate core recovered, with adjacent numbers indicating core numbers (R indicates the core type, rotary core barrel). VE: vertical exaggeration, m bsl: meters below sea level, and m bsf: meters below sea floor. (c–e) Core images of faults FZ697, FZ720, and FZ801. The white arrows show the inferred sense of the faults (Chester, Mori, et al., 2013; Kirkpatrick et al., 2015).

Features of fluidized granular flow, mirror fault surfaces, clast-cortex aggregates, coseismic crystal plastic deformation, and amorphous material, are scrutinized in the first approach, recently reviewed by Rowe and Griffith (2015). However, these coseismic slip structures are very uncommon for the majority of faults developed in sedimentary rocks, despite that the majority of the large earthquakes are associated with subducted sediments (Lay & Bilek, 2007). This makes it hard to diagnose the record of most subduction zone earthquakes through recognition of the coseismically produced structures.

The second approach is focused on how much frictional heating was induced by seismic slip, which constitutes by far the largest part (~80 to 90%) of the total earthquake energy budget (e.g., Scholz, 2002). Frictional heating quickly results in elevated temperatures (Rice, 2006) and induces thermochemical reactions within a fault zone. Identifying signatures of frictional heating is thus an attractive way to diagnose earthquake slip. Among the frictional-heating proxies, pseudotachylyte, which is a solidified melt product of rapid frictional heating, is widely considered a reliable indicator of past earthquakes (Cowan, 1999), and also referred to as so-called "fossilized earthquake" (Lin, 2008). However, pseudotachylyte is rare in the upper segments of most faults (spanning the topmost few kilometers of the crust), where the friction melt window is not reached as rupturing proceeds without inducing a melt phase due to the lower confining stresses (e.g., Sibson & Toy, 2006; Swanson, 1992). This is primarily related to the high temperatures required to produce melt rock.

Recently, alternative approaches were developed to detect seismic frictional heating with peak temperatures below the melting temperature of fault rock. These include frictional devolatilization of carbonates and hydrous silicates (e.g., Han et al., 2007; Rowe et al., 2012), trace element partitioning (e.g., Tanikawa et al., 2015), and maturation of organic matter (e.g., Savage et al., 2014). However, each of these approaches can only be applied under specific conditions, and sometimes detect a certain temperature range only (see Yang et al., 2016, for details). Thus, to achieve a complete picture of frictional heating, yet other approaches are desired, either independent of or working in concert with existing methods. This would aid diagnosing earthquake slip in rock records. Here we document a mineral-magnetic method based on the occurrence of pyrrhotite (Fe_7S_8), a magnetic mineral that derives from the heating of pyrite (FeS_2).

Pyrite is probably the most widespread sulfide mineral in the Earth's crust (e.g., Craig & Vokes, 1993), and also is ubiquitous in fault zones (e.g., Chou, Song, Aubourg, Song et al., 2012; Togo et al., 2011; Zheng et al., 2002). It has been documented that pyrite is thermally unstable and is readily decomposed to pyrrhotite at elevated temperatures of over 300–500°C in various atmospheres at different pressures (Bhargava et al., 2009; Hu et al., 2006; Lambert et al., 1998). Pyrite is a paramagnetic mineral. The newly formed pyrrhotite is either hexagonal (nominally antiferromagnetic at low temperature; the long-term fate of quenched-in ferrimagnetic pyrrhotite structures, however, is unknown) or monoclinic (ferrimagnetic) (e.g., Dekkers, 1988). This enables detection of monoclinic pyrrhotite in trace amounts with sensitive magnetic methods. If seismic frictional heating induces a sufficiently elevated temperature, the new pyrrhotite formed at the expense of preexisting pyrite leaves an increased "magnetic footprint" in fault rocks. This yields a distinctive magnetic record of seismic slip in fault zones, even when only trace amounts of pyrite are originally present. It should be realized that it is not straightforward to establish this pyrite-pyrrhotite transformation by routinely applied geochemical analysis due to the low concentration ($<$0.1%) and small grain size (a few tens of micrometers at most) of both original and newly formed minerals. Rock magnetic techniques are capable of determining the nature, size, and concentration of magnetic minerals in a sample down to the ppm level. Earthquake slip records may thus be traced by identification of the magnetic mineral assemblages within a fault zone.

During the IODP expedition 343, JFAST successfully drilled at Site C0019 and collected approximately 55 m of discontinuous core in the interval of 175–835 m below sea floor (bsf) spanning the frontal prism, plate-boundary fault zone (décollement), and underthrust sediments (Chester, Mori, et al., 2013). X-ray diffraction analysis revealed that pyrite is widely present in the core samples (Chester, Mori, et al., 2013). Multiple localized slip surfaces have been identified in cored sediments (Chester, Rowe, et al., 2013; Keren & Kirkpatrick, 2016; Kirkpatrick et al., 2015; Rabinowitz et al., 2015). Through access to the cored material, we can examine with mineral magnetic methods whether or not pyrrhotite occurs next to pyrite in the core sediments in and nearby those slip surfaces. This allows us to study their association with frictional heating induced by high-velocity seismic slip.

2. Geological Background and Sample Materials

The IODP Site C0019 is located approximately 250 km off the Pacific coast of Honshu, Japan, and approximately 93 km seaward of the epicenter of the 2011 Tohoku-oki earthquake (Figure 1a). The site is ~6 km landward of the Japan Trench axis, where the Pacific Plate subducts beneath the North American Plate with a rate of 85 mm/year (Argus et al., 2011). This rapid convergence results in extensive seismic activity. The historical record for the region includes 13 magnitude (M) 7 and 5 M8 earthquakes over the last 400 years (e.g., Kanamori et al., 2006), in addition to the 2011 Mw 9.0 event and its aftershock sequence.

The retrieved cores are composed of sediments from the accretionary wedge or prism and the downgoing plate; they were grouped into seven lithologic units (Figure 1b). Units 1–3 are prism sediments and comprise mainly mudstone and siliceous mudstone. Unit 4 mostly consists of strongly sheared clays and is interpreted as the décollement zone. Units 5–7 are underthrust sediments, including brown mudstone in Unit 5, pelagic clay in Unit 6, and laminar chert in Unit 7. Chester, Mori, et al. (2013) provide detailed descriptions of each unit. Multiple fault zones are identified above and below Unit 4, the plate-boundary fault zone (Figure 1b); they are important as well in understanding the slip history of the plate boundary (Chester, Rowe, et al., 2013; Keren & Kirkpatrick, 2016; Kirkpatrick et al., 2015; Rabinowitz et al., 2015).

For this study, 40 samples were collected from the interval of 688.63–802.18 m bsf in the frontal prism sediments of Unit 3. The samples cover three major fault zones: FZ697, FZ720, and FZ801 (Figure 1b). In an X-ray computed tomography image (Figure 1c), FZ697 at 697.82 m bsf is characterized as an ~2–7 mm thick bright band with a dip of 10° relative to the horizontal. FZ720 is defined as a high conductivity zone in the resistivity logs between 719 and 725 m bsf, where beds are truncated and crosscut by a zone of deformed rock containing multiple narrow shear surfaces and incoherent bedding (Figure 1d, see also Chester, Mori, et al., 2013). FZ801 at 801.04 m bsf is defined by a dense array of millimeter-thick seams of fault rock that are inferred to be shearing fractures given the lack of continuity in the mudstone sedimentary fabric (Figure 1e).

3. Methods

The natural remanent magnetization (NRM) of all samples was measured with a Model SMD-88 spinner magnetometer (Natsuhara Giken Co., Ltd.) with an instrumental noise level of ~10^{-8} Am^2 installed in the paleomagnetism laboratory onboard the D.V. *Chikyu* during Expedition 343. All other magnetic measurements at room temperature were conducted postcruise at the Key Laboratory of Seismic Observation and Geophysical Imaging, Institute of Geophysics, China Earthquake Administration (Beijing, China). Low-field magnetic susceptibility (expressed on a mass-specific basis as χ) was measured with an MFK1-FA Multi-Function Kappabridge susceptometer (AGICO, Brno, Czech Republic) with a detection limit of 2×10^{-8} SI and a measurement accuracy of 0.1%, at a frequency of 976 Hz and in a field of 200 A/m (peak to peak). Magnetic hysteresis loops and back-field isothermal remanent magnetization (IRM) curves were acquired to determine the hysteresis parameters, coercive force (B_c), remanence coercive force (B_{cr}), saturation remanence (M_{rs}), and saturation magnetization (M_s) using a MicroMag™ Model 3900 vibrating sample magnetometer (VSM, Princeton Measurements Corp.), with a maximum applied field of 1.0 T. First-order reversal curves (FORCs) (Roberts et al., 2000) were measured with the VSM 3900 to evaluate magnetostatic interactions and further assess the magnetic domain state. For each FORC diagram, 120 curves were measured with an averaging time of 0.5–1 s per data point and a field increment of 4 mT. FORC diagrams were processed using the FORCinel package (Harrison & Feinberg, 2008) to identify regions of the FORC distribution.

Low-temperature magnetic measurements (down to 5 K) were conducted with a SQUID magnetometer (MPMS XL-7, Quantum Design Inc., CA) with a sensitivity of 10^{-11} Am^2 for 10 selected samples of a mass ranging between 120 and 150 mg at the State Key Laboratory for Artificial Microstructure and Mesoscopic Physics, Peking University (Beijing, China). Three different measurement cycles were carried out for each sample. A zero-field-cooled cycle was applied first, where the sample was cooled down to 5 K from room temperature (300 K) in a zero field. Then, an IRM was imparted using a 2.5 T field. The field was subsequently switched off, and the IRM was measured each 5 K during warming back to 300 K. A field-cooled cycle was then applied, by cooling the sample from 300 down to 5 K in the presence of a 2.5 T field, which was switched off before warming sample back to 300 K. Again, the IRM of the sample was measured at 5 K intervals during warming back to 300 K. Finally, a room temperature saturation isothermal remanent magnetization (RT-SIRM) cycle was measured, where a 2.5 T SIRM was imparted at 300 K. The samples' remanence was measured at 5 K steps during cooling down to 5 K and warming back to 300 K in a zero magnetic field.

Magnetization versus temperature of 24 representative samples was measured in air by a modified horizontal translation-type Curie balance at the Paleomagnetic Laboratory Fort Hoofddijk, Utrecht University (Netherlands), with a sensitivity of approximately 5×10^{-9} Am^2 (Mullender et al., 1993). Between ~40 and ~70 mg of powdered sample was put into a quartz glass sample holder and held in place by quartz wool; heating and cooling rates were 6 and 10°C/min, respectively. Stepwise thermomagnetic runs were carried out with intermittent cooling to 100°C lower than the maximum temperature of each segment. The

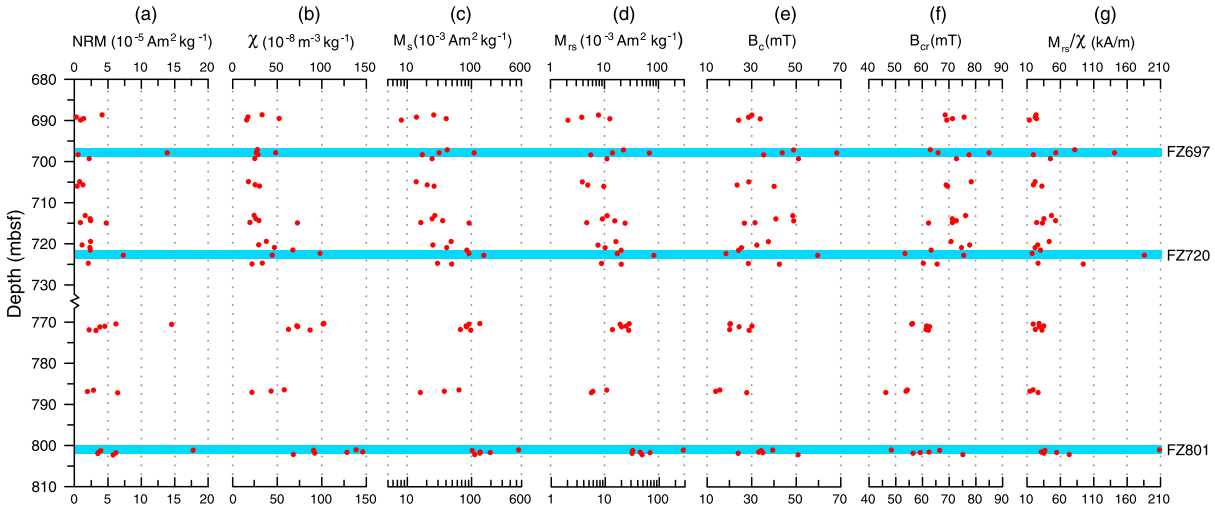

Figure 2. Magnetic properties of prism sediments (680–810 m bsf) from the JFAST borehole C0019E. (left to right) Downhole (a) natural remanent magnetization (NRM), (b) mass-specific low-field magnetic susceptibility (χ), (c) saturation magnetization (M_s), (d) saturation remanence (M_{rs}), (e) coercive force (B_c), (f) remanent coercive force (B_{cr}), and (g) ratio between M_{rs} and χ. The blue bars indicate the locations of the three fault zones.

maximum temperatures of the successive heating segments were 150, 250, 400, 520, 620, and 700°C, respectively.

Polished thin sections from nine representative samples were analyzed for magnetic minerals with an Ultra Plus field emission scanning electron microscope (SEM, Carl Zeiss, Germany) operated at 15 kV at the Key Laboratory of Metallogeny and Mineral Assessment, Ministry of Land and Resources (Beijing, China). Elemental compositions were determined from point analyses of individual mineral grains by the attached energy dispersive X-ray spectrometer (EDS, Oxford IE350 X-Max), using an Oxford Instruments INCA EDS microanalysis system (Oxford Instruments, UK).

4. Results

4.1. Rock Magnetism

Downhole magnetic parameters of sediment samples are shown in Figure 2. NRM is generally $\lesssim 5 \times 10^{-5}$ Am^2 kg^{-1} throughout the studied interval, except for the aforementioned three fault zones and another at a depth of 770.44 m bsf where the NRM is 15–17 $\times 10^{-5}$ Am^2 kg^{-1}, that is, ~3 times higher (Figure 2a and Table S1 in the supporting information). The magnetic signature of the sample at 770.44 m bsf appears to be dominated by pseudo-single-domain (PSD) magnetite (Figure S1); it is inferred to be a volcanic ash. There appears to be no slip surface present after close reexamination. Pyrrhotite is not identified as well. Figure 2 also shows that samples from the three fault zones have relatively higher χ, M_s, M_{rs}, B_c, and B_{cr} values compared to their host sediments (Figures 2b–2f and Table S1). For example, the host sediments show a distinctly variable M_s (from 8.1 to 195.7 $\times 10^{-3}$ Am^2 kg^{-1}) with an average and standard deviation of 60.4 $\times 10^{-3}$ and 45.6 $\times 10^{-3}$ Am^2 kg^{-1}, respectively (n = 35). In contrast, M_s of the fault zone sediments is much higher, ranging from 31.5 $\times 10^{-3}$ to 541.6 $\times 10^{-3}$ Am^2 kg^{-1} with an average value (±standard deviation) of 176.2 ± 210.5 $\times 10^{-3}$ Am^2 kg^{-1} (n = 5) (Table S1). It is noteworthy that the fault zones have markedly higher M_{rs}/χ values (>60 kA/m), whereas the M_{rs}/χ values of host sediments are predominately lower than 30 kA/m (Figure 2g; the sample at 770.44 m bsf has a M_{rs}/χ value of 19.2 kA/m).

Hysteresis loops of fault zone samples (Figures 3b and 3c and S1b and S1c in the supporting information) are much "wider" than those of their host samples (Figures 3a and 3d and S1a and S1d), compatible with their higher B_c values (Figure 2e). However, all loops are closed and approach magnetic saturation in a field of ~300 mT, indicating that the magnetic minerals are dominated by low-coercivity ferrimagnetic minerals. A scatterplot of M_{rs}/χ versus B_{cr} provides a first-order assessment of the magnetic mineralogy (Peters & Thompson, 1998). All host sediments form a tight cluster within the (titano) magnetite area, whereas the majority of fault zone sediments are located in the pyrrhotite area (Figure 4).

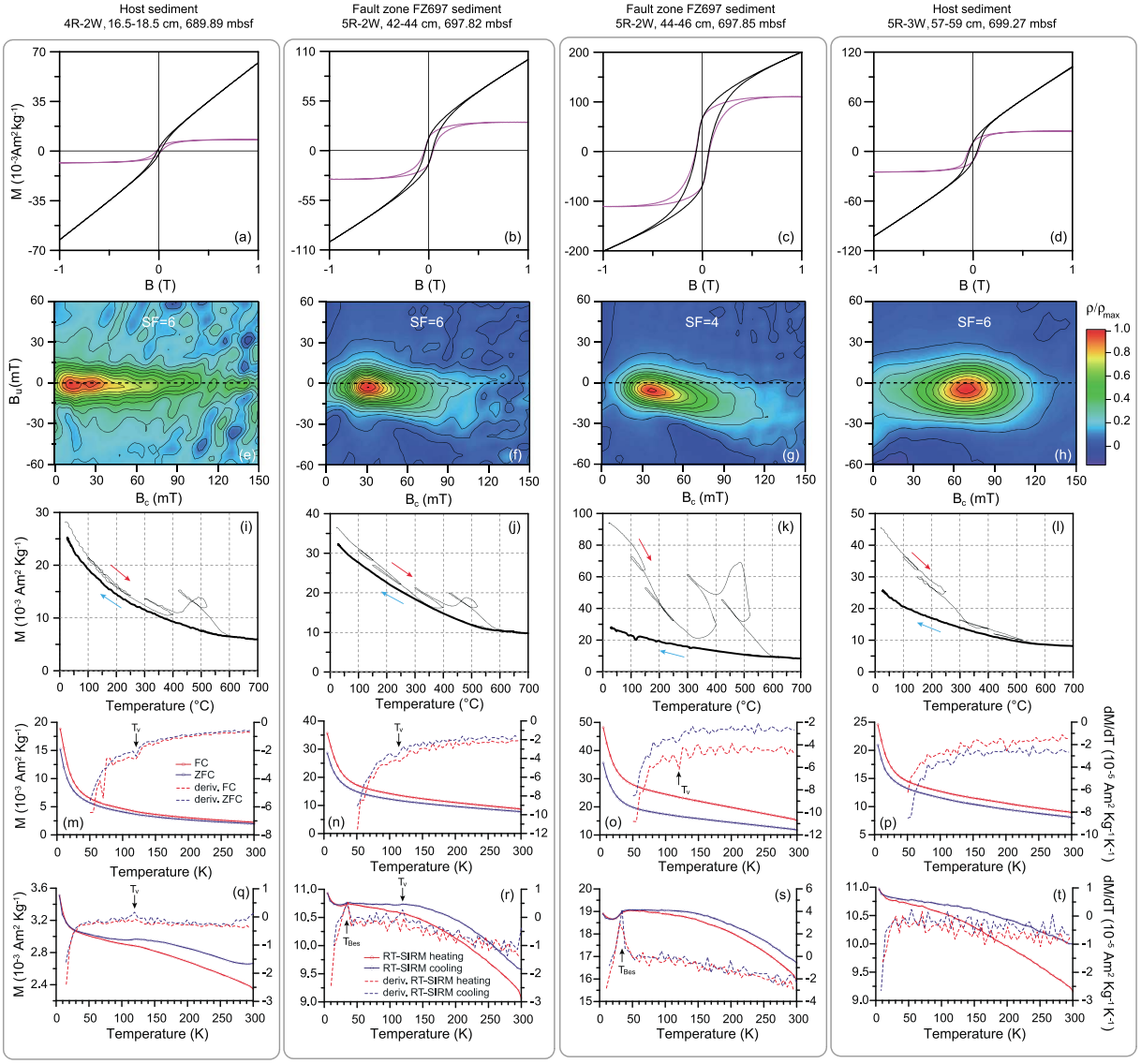

Figure 3. Rock magnetic properties of representative fault zone and host sediment samples from the fault FZ697. (a–d) Hysteresis loops before (dark lines) and after (magenta lines) correction for the paramagnetic contribution. (e–h) First-order reversal curve (FORC) diagrams processed with the FORCinel package (Harrison & Feinberg, 2008); the VARIFORC option was not used. For each sample, the optimal smoothing factor (SF) was calculated and applied. Each diagram is scaled to its maximum FORC density (ρ_{max}). (i–l) Stepwise thermomagnetic analyses performed with a modified horizontal translation Curie balance (Mullender et al., 1993). (m–p) Warming curves from 5 to 300 K of a 2.5 T IRM imparted in samples at 5 K. ZFC (zero-field-cooled) and FC (field-cooled) isothermal remanent magnetizations (IRMs) curves are shown in blue and red, respectively, and the corresponding temperature derivatives with blue and red dashed lines. (q–t) Low-temperature cycling curves of a 2.5 T IRM imparted in samples at room temperature (RT-SIRM). The cooling curves are shown in blue and the warming curves in red. Temperature derivatives of the remanence during cooling and heating are shown with blue and red dash lines, respectively.

FORC diagrams (Figures 3e–3h and S1f–S1i) also illustrate these differences. In general, two types are identified for host sediments. In large majority (Figures 3e and S1f and S1i) they show FORC diagrams characterized by contours that start to diverge away from the origin, with elongated and closed contours toward higher coercivities. Some asymmetry is noticeable. This contour pattern is consistent with the behavior of typical interacting magnetic particles in the PSD state (Pike et al., 1999; Roberts et al., 2014), which is recently suggested to be equivalent to the "vortex state" (Roberts et al., 2017). FORC diagrams for other host sediments occasionally exhibit closed concentric contours with a peak B_c value of 60–70 mT, and the concentric contours show a marked vertical spread and a shift to negative interaction fields (Figure 3h). All of these features are consistent with those of single-domain (SD) greigite with strong magnetic interaction (e.g., Roberts et al., 2011). FORC distributions of fault zone sediments are characterized by a B_c peak centered at 30–40 mT

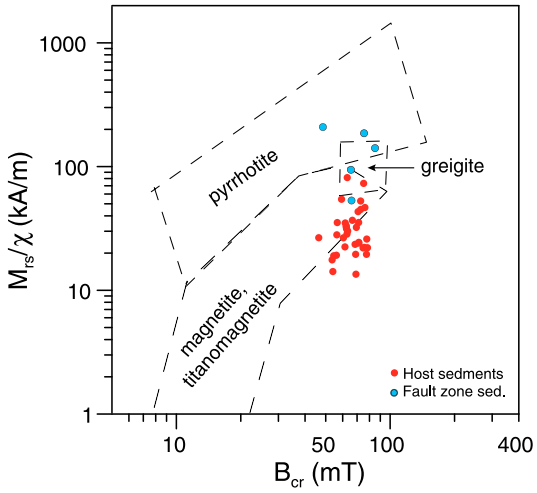

Figure 4. *X-Y* plot of magnetic parameters B_{cr} versus M_{rs}/χ of core sediments. Boxes with typical parameter ranges for the different magnetic minerals were redrawn from Peters and Thompson (1998).

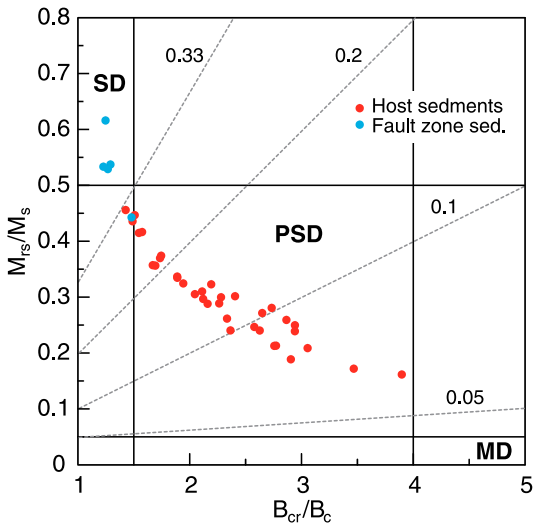

Figure 5. Day plot of the hysteresis ratios M_{rs}/M_s and B_{cr}/B_c of core sediments. Single-domain (SD), pseudo-single-domain (PSD), and multidomain (MD) boundaries are after Day et al. (1977). The dashed lines indicate contours of the parameter D_{JH}, $(M_{rs}/M_s)/(B_{cr}/B_c)$ (Housen & Musgrave, 1996).

(Figures 3f and 3g and S1g and S1h), with a prominent "kidney" shape toward higher coercivities, suggesting the occurrence of SD pyrrhotite (Larrasoaña et al., 2007; Roberts et al., 2014; Wehland et al., 2005).

High-temperature thermomagnetic measurements for the majority of sediments show a monotonous decay in magnetization from room temperature until approximately 400°C, at which point the magnetization starts to increase and peaks at ~500°C (e.g., Figures 3i–3k and S1k and S1l). This probably results from Fe-bearing clay minerals or pyrite altering to a new ferrimagnetic phase. After this peak the magnetization decays linearly until 580–600°C, indicating the presence of magnetite (Dunlop & Özdemir, 1997). In fault zone sediments, a more distinct drop around 320°C in magnetization (Figures 3j and 3k and S1l and S1m) is attributed to a more prominent contribution from fine-grained (monoclinic) pyrrhotite to the signal (in addition to that of magnetite). Further, a more rapid decay in magnetization above ~200°C is observed on the heating curve for some of the host sediments (Figure 3l). It may be linked to the thermal decomposition of thermally unstable greigite (Torii et al., 1996).

Results of the low-temperature magnetic measurements display different characteristic behavior depending on the respective sample levels. For the host sediments, two types of low-temperature warming curves are identified, and these correlate with two of the previously identified types of FORC diagrams. Most of them show a weak Verwey transition (T_v) at ~120 K on the zero-field-cooled/field-cooled curves (Figures 3m and S1p and S1s) and RT-SIRM curves (Figures 3q and S1u). This indicates that magnetite, probably of PSD/multidomain (MD) size, is present, as the remanence is not fully recovered on warming back to 300 K (e.g., Muxworthy & McClelland, 2000; Özdemir et al., 2002). These results corroborate the hysteresis loop and FORC diagram data. In ensemble they indicate that low-coercivity ferrimagnetic PSD/MD magnetite is a foremost magnetic mineral in the host sediments. The greigite-bearing host sediments (e.g., sample 5R-3W, 57–59 cm, 699.27 m bsf) show no visible low-temperature phase transition on RT-SIRM curves (Figure 3t), which is compatible with the presence of greigite (Dekkers et al., 2000; Roberts et al., 2011), as indicated by its FORC diagram (Figure 3h) and thermomagnetic behavior (Figure 3l). For fault zone sediments, the RT-SIRM curves drop significantly at ~35 K on both of cooling and heating curves (Figures 3r and 3s and S1v and S1w). This corresponds to the Besnus transition (T_{Bes}) of pyrrhotite (Dekkers et al., 1989; Rochette et al., 1990; Volk et al., 2016). The remanence is almost fully recovered during warming over this temperature, suggesting that pyrrhotite is SD sized (Dekkers et al., 1989; Rochette et al., 1990). These observations concur with the Day plot (Day er al., 1977; Figure 5), where the host sediments lie mainly in the PSD field, and most of the fault zone samples are located in the region with D_{JH}, that is, $(M_{rs}/M_s)/(B_{cr}/B_c)$, >0.33, which concurs with the occurrence of SD pyrrhotite (Housen & Musgrave, 1996).

4.2. SEM Observations and EDS Analyses

SEM observations (Figure 6) and EDS analyses (spectra of selected spots shown in supporting information Figure S2) revealed that pyrite appears to be abundant in all sediments. Both clustered (Figures 6a and S2a–S2c) and isolated (Figures 6b and S2d) pyrite framboids occur. Magnetite grains with variable Ti contents are found in most samples (Figures 6c and S2e). Greigite occasionally occurs as small interstitial grains within cleavages of sheet silicate grains (Figures 6d and S2f), associated with a protracted late diagenetic greigite growth (Aben et al., 2014; Roberts & Weaver, 2005). Pyrrhotite is identified only in samples from the three fault zones. Three typical modes of

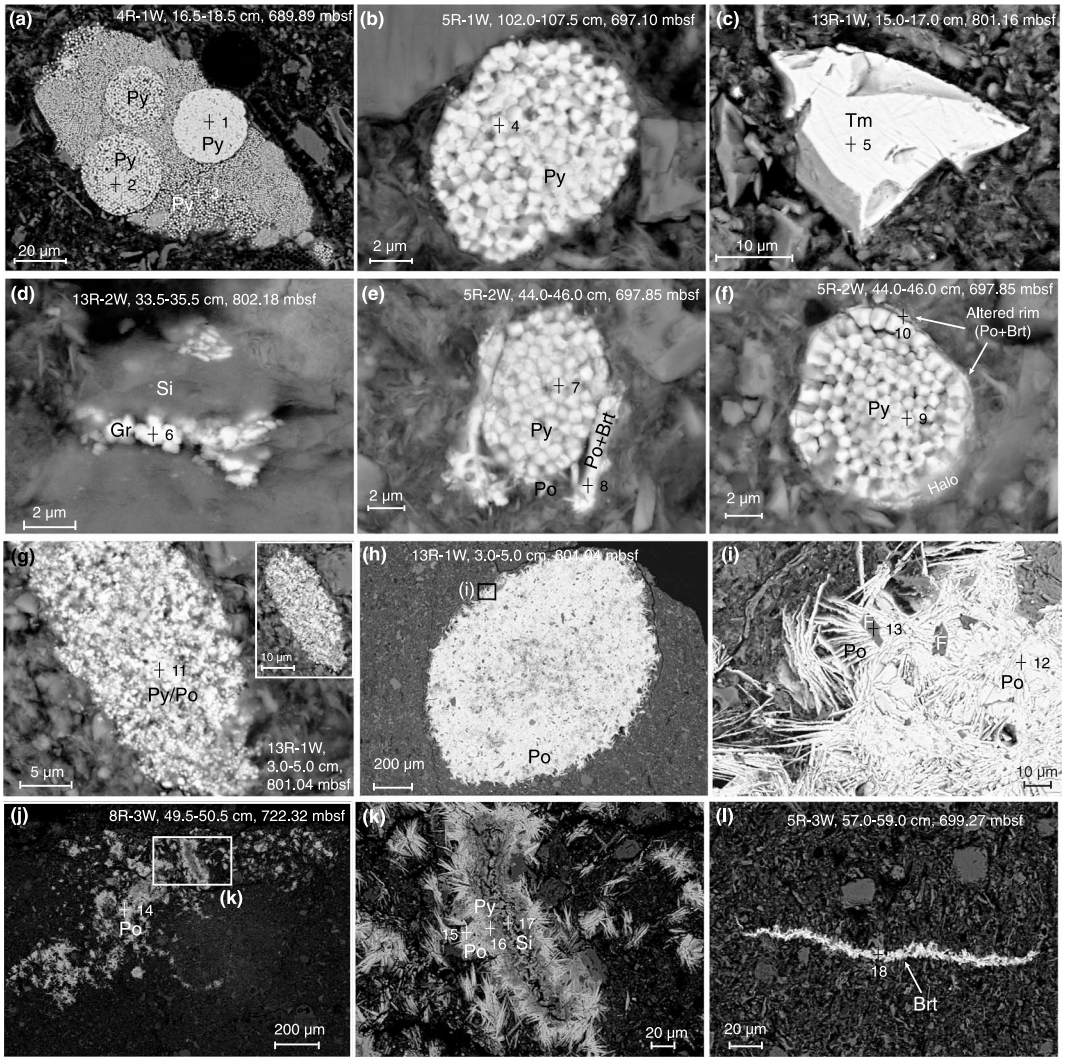

Figure 6. Back-scattered scanning electron microscope images of selected samples. (a) Polyframboidal pyrite (Py) aggregate with space-filling pyrite grains. (b) Spherical pyrite framboids (Py). (c) Example of titanomagnetite grains with variable Ti contents (Tm). (d) Sample containing greigite (Gr) that grows between the cleavage planes of an iron-bearing detrital sheet silicate (Si). (e and f) Framboidal pyrite with altered rim consisting of intergrowths of pyrrhotite (Po) and barite (Brt). A distinctive halo surrounds the particle. (g) Disaggregated pyrite with visible original framboidal morphology. It has a heterogeneous Fe/S ratio (~0.5 to ~1), suggesting a mixture of pyrite and pyrrhotite (Py/Po). (h and i) Nodule with a fibrous or spiky exterior surface formed by pyrrhotite (Po) laths that are tightly clustered along edges of feldspar (F) clasts. (j and k) Acicular pyrrhotite (Po) around the edges of silicates (Si). Pyrite (Py) occurs more toward the center of the silicates. (l) Barite chains filling the fracture of silicates. The numbered plus symbols indicate the EDS analysis spots, with spectra shown in Figure S2 in the supporting information.

occurrence are identified: The first mode includes altered rims surrounding framboidal pyrite (Figures 6e and 6f and S2g and S2i) or disaggregated pyrite (Figure 6g). The altered rim consists of intergrowths of pyrrhotite and barite as revealed by EDS analyses (Figures S2h and S2j), which sometimes is surrounded by distinctive halos (Figure 6f). The disaggregated pyrite, of which the original framboidal morphology can still be visible (inset, Figure 6g), has a heterogeneous Fe/S ratio, ranging from ~1 to ~0.5 (Figure S2k). It seems a mixture of pyrite and pyrrhotite, suggesting that the pyrite underwent a phase transformation to pyrrhotite. The second mode is pyrrhotite also occurring as nodules with variable shape and large size (up to about 1 mm) (Figure 6h). At higher magnifications, the nodules have a fibrous or spiky exterior surface, comprising tightly clustered pyrrhotite laths along the edge of feldspar grains (Figures 6i and S2l and S2m). They are oriented at high angles to the feldspar surface and extend up to several tens of micrometer. The third mode is more rare.

Acicular pyrrhotite (Figures 6j and S2n) occurs along the peripheral regions of fractures cutting silicates mass, with pyrite toward the center part (Figures 6k and S2o–S2q). Another significant feature for the fault zone sediments is the occasional presence of chains of barite rosettes (Figures 6l and S2r).

5. Discussion

5.1. Mechanisms of Pyrrhotite Formation Within Fault Zones

The combination of above-mentioned mineral magnetic properties and SEM/EDS observations provides compelling evidence for the presence of monoclinic pyrrhotite confined to within the three narrow fault zones. In contrast, the plate-boundary fault zone, which is composed mostly of scaly clays, is dominated by magnetite (see Yang et al., 2016, for details). This difference could be due to the extreme physical/chemical conditions in active plate-boundary fault zones, compared to the overlying wedge sediment sections (Sutherland et al., 2017), although further work is required to confirm this explanation.

It is known that pyrrhotite may form by prolonged heating pathways, such as reaction of magnetite and pyrite at low-temperature ($<$200°C) as a result of burial diagenesis and anchimetamorphism (Gillett, 2003). It may also form by thermochemical sulfate reduction (Manning & Elmore, 2015). The magnetic susceptibility of magnetite is much higher (~20 times) than that of pyrrhotite (Peters & Dekkers, 2003). Formation of pyrrhotite at the expense of magnetite would thus lead a significant decrease in magnetic susceptibility of the sediments, which is not observed (Figure 2b). Thermochemical sulfate reduction occurs at high diagenetic temperatures (160–180°C) and over longer time intervals, from several tens of thousands to a few millions of years (Machel, 2001). The sediments studied here are mostly late Pliocene to Pleistocene in age (Chester, Rowe, et al., 2013) and lack the necessary long-lasting heat sources. Therefore, prolonged-heating mechanisms are not viable to explain the formation of pyrrhotite.

Multichannel seismic profiles in the vicinity of the drill site do not indicate a gas-hydrate-related bottom-simulating reflector (i.e., high-amplitude reflectors and reversed polarity; cf. Hyndman and Spence, 1992) above the décollement, suggesting that there are no potential hydrocarbon traps or methane hydrate zones in the sediments (CEDX, 2012). Therefore, migration of hydrocarbons (e.g., Abubakar et al., 2015) and gas-hydrate-associated methane (Housen & Musgrave, 1996; Kars & Kodama, 2015; Larrasoaña et al., 2007) also cannot explain the presence of pyrrhotite only within the three fault zones.

This leaves thermal breakdown of pyrite (Bhargava et al., 2009; Lambert et al., 1998) or discharge of hydrothermal fluids (Urbat et al., 2000) as plausible scenarios to form pyrrhotite in the fault zones. Drivers are frictional heating and related hydrothermal fluids during the very short-duration high-velocity seismic slip. Multiple slip surfaces indicate that earthquake slip occurred repeatedly in the subduction history of the incoming Pacific Plate (Chester, Rowe, et al., 2013; Keren & Kirkpatrick, 2016; Kirkpatrick et al., 2015; Rabinowitz et al., 2015). In addition to the latest 2011 event and its aftershock sequence, a series of $>$M7-class earthquakes have been recorded at the Japan Trench during the last decades (Kanamori et al., 2006). We discuss below thermodynamic and kinetic aspects of the transformation of pyrite to pyrrhotite to constrain the cumulative temperature effect of seismic slip.

5.2. Seismic Frictional Heating and Pyrite Reaction During an Earthquake

The amount of frictional heat generated during earthquake rupturing has been debating for over 50 years (e.g., Brune et al., 1969; Lachenbruch & Sass, 1980), despite the fact that frictional heat is thought to be the largest part (80–90%) of the total seismic energy budget (e.g., Scholz, 2002). Direct temperature measurements across fault zones have been conducted during the several recent fault zone drilling campaigns carried out shortly after major earthquakes, for example, the Taiwan Chelungpu-fault Drilling Project (Kano et al., 2006), the Wenchuan Earthquake Fault Zone Scientific Drilling Project (Li et al., 2015), and JFAST (Fulton et al., 2013). All of them revealed a very weak bulk temperature anomaly ($<$0.5°C), which is much lower than the prediction from in situ stress measurements and laboratory data of rock friction. However, the local temperature within the slip zone could have been elevated significantly by coseismic frictional heating, even at shallow crustal levels. This follows from the often observed thermally activated chemical reactions in slip zones, including dehydration reactions (e.g., Brantut et al., 2011; Hirose & Bystricky, 2007), decarbonation reactions (e.g., Han et al., 2007; Sulem & Famin, 2009), trace element partitioning features (e.g., Ishikawa et al., 2008; Tanikawa et al., 2015), graphitization of carbonaceous materials (e.g., Kuo et al., 2017; Oohashi

et al., 2011), and thermal maturation of organic molecules (e.g., Rabinowitz et al., 2017; Savage et al., 2014). Local melting, as evidenced by the presence of glass (pseudotachylyte), has also been reported in both natural and experimentally simulated slip zones (Kuo et al., 2016, and references therein). All of these arguments indicate that short-duration frictional heating can locally induce significant temperature anomalies within slip zones (at the scale of a few millimeter or even less). However, as evident by the aforementioned faint bulk temperature anomalies around seismically active faults or by the lack of bulk pseudotachylytes, the average frictional heat over an entire fault zone could still be rather low. This may be explained by dynamic weakening mechanisms (e.g., flash heating and thermal [thermochemical] pressurization) or extra heat sinks (e.g., phase transitions of pore water and endothermic chemical reactions) (e.g., Chen, Niemeijer Fokker, 2017; Chen, Niemeijer, & Yao, 2017, and references therein). As mentioned, pyrite is thermally unstable and readily decomposed to pyrrhotite at elevated temperatures. Below we demonstrate the occurrence of pyrite-pyrrhotite reaction induced by frictional heating generation during an earthquake through a numerical modeling experiment.

The potential temperature rise due to frictional heating within these fault zones during an earthquake is estimated using a finite element method implemented in the COMSOL Multiphysics software package (version 3.5), following similar procedures as reported previously (e.g., Chen et al., 2013, 2016). Details about the modeling process can be found in supporting information Text S1 (Bayer, 1973; Chester, Mori, et al., 2013; Fine & Millero, 1973; Fulton et al., 2013; Lin et al., 2014; Sibson, 2003; Tanikawa et al., 2013; Ujiie et al., 2016). The numerical results show that frictional heating induces a temperature rise from the beginning of the fault slip. For a shear stress of 0.8 MPa, the temperature reaches nearly 710°C within a slip zone of 1 cm thick (Figure 7a), and over 1,000°C within a slip zone of 0.5 cm thick (Figure 7b) after 25 m of slip, respectively. Thinner slip zones, and larger shear stress as well, will thus induce higher temperature increases (Figures 7a and 7b). In the drill cores, indications of temperature rise due to rapid seismic slip have also been found at several horizons above and below the plate-boundary fault zone by Rabinowitz et al. (2013), using thermal maturity of biomarkers. Although they examined other faults than we do here, this finding suggests that the approximately ~3 km of total slip recorded in the JFAST boreholes was distributed over several discrete faults in a rather wide interval ($>$30 m) (Scholz, 2014); it was not confined to the plate-boundary fault zone only.

To assess whether frictional heating can induce a reaction of pyrite to pyrrhotite, we calculated the kinetics of the pyrite-pyrrhotite reaction, under the premise of an Arrhenius-type kinetic reaction (Hoare & Levy, 1990; see supporting information Text S1 for details). For a shear stress of 0.8 MPa, the fraction of pyrrhotite formed at the expense of pyrite is ~0.1 within a slip zone of 1 cm after 25 m slip (Figure 7c); the reaction could be entirely completed during seismic slip in a slip zone with a width of 0.5 cm (Figure 7d). It is noteworthy that once the reaction is significantly activated, it proceeds even after the slip event itself has terminated. For example, the reacted fraction reaches ~0.26 after 25 m slip (or 25 s, as the slip velocity is 1 m/s) in a slip zone of 1 cm thickness with a shear stress of 0.8 MPa (Figures 7c and 7e). The reaction of pyrite appears to be primarily controlled by temperature (see equation (S9) in Text S1). It is predicted to start with the very beginning of the slip and the reaction proceeds with increasing temperature (Figure 7e). It is, however, extremely slow below ~640°C; at that temperature the reacted pyrite fraction is only ~0.005 (Figure 7e, inset). This is in line with the finding that formation of stable pyrrhotite commences initially when pyrite is heated in an argon atmosphere to above ~560°C, and steps up when the temperature is over ~630°C (Li & Zhang, 2005). When the temperature is over ~640°C, the pyrite-pyrrhotite reaction accelerates, and is complete at ~800°C (Figure 7e). The portion of reacted pyrite is influenced by the distribution of frictional heat: the chemical reaction is enhanced only within the slip zone (Figure 7f). Also, it can be completed in several seconds to tens of seconds (Figure 7f). All these modeling results demonstrate that the elevated temperature due to frictional heating and associated coseismic hydrothermal fluids can induce alteration of preexisting pyrite within fault zone sediments. Here the temperature experienced by these fault zones is likely less than 800°C, as an incomplete pyrite break-down reaction is often observed in the fault zone sediments (e.g., Figures 6e–6g). Postseismic fluids might also induce pyrrhotite formation. However, the fluid temperature is a crucial controlling factors, and, as suggested by the above-mentioned pyrite-pyrrhotite reaction modeling, the reaction is extremely slow below ~640°C (Figure 7e) for short-duration pyrrhotite formation. It should be realized that prolonged percolation of warmer fluids would leave veinlets (often quartz-rich) with larger crystals, something which is never observed here. Also, the highest temperature currently reported for submarine

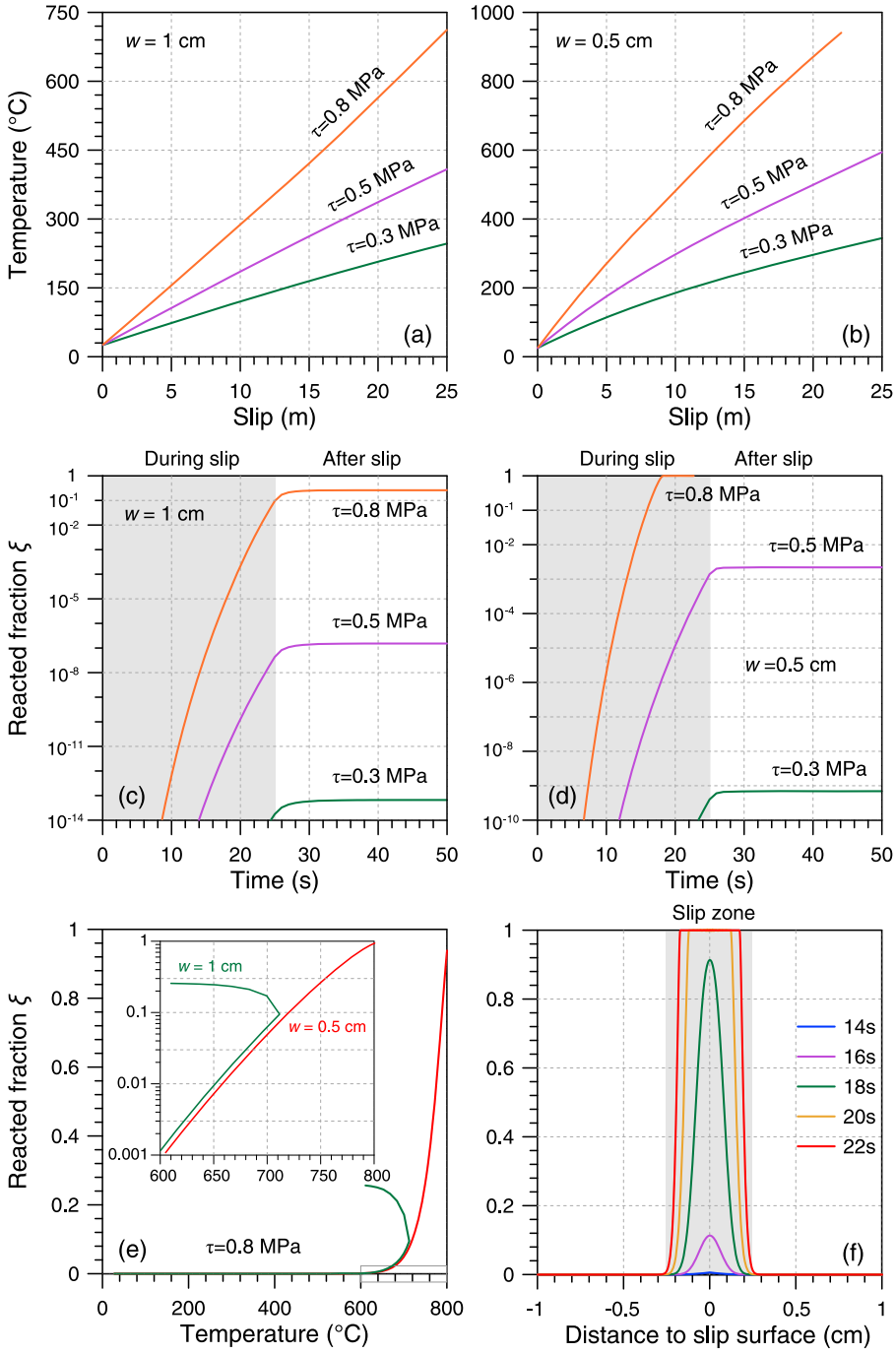

Figure 7. Modeled temperature change induced by earthquake frictional heating during slip of 25 m in a slip zone of (a) 1 cm and (b) 0.5 cm thickness (w) for various shear stresses (τ = 0.3, 0.5, and 0.8 MPa) using a finite element method (see supporting information Text S1 for details). The fraction of pyrite reacted away predicted by kinetic analysis at the center of the slip zone with a thickness of (c) 1 cm and (d) 0.5 cm for various shear stresses (see supporting information Text S1 for details). (e) The reacted pyrite fraction as a function of temperature in slip zones with τ = 0.8 MPa, and w = 1 and 0.5 cm, respectively. The inset is an enlarged portion of the panel ($T > 600$°C). (f) Snapshots of the distribution of reacted fraction of pyrite at different time after the beginning of slip across a fault core with τ = 0.8 MPa, and w = 0.5 cm, respectively.

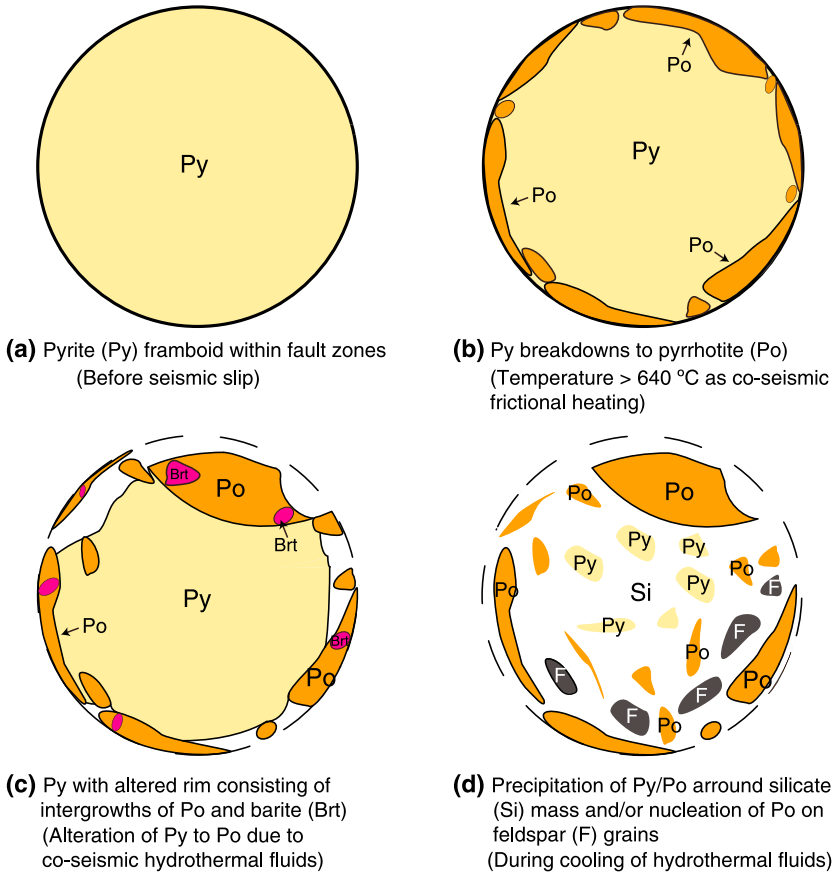

Figure 8. A cartoon showing the pyrite reaction and pyrrhotite formation during an earthquake. During the seismic slip, (a) the preexisting pyrite in the slip zone decomposes to pyrrhotite when the temperature is over ~640°C as modeled with chemical kinetics, and (b) a pyrrhotite rim surrounding the pyrite core is formed when the reaction is incomplete. (c) Leached by coseismic hot fluids, pyrite is altered and a rim consisting of intergrowths of pyrrhotite and barite is formed. (d) With cooling of the coseismic hot fluids, pyrite/pyrrhotite precipitates around the silicates, and/or pyrrhotite nucleated on feldspar grains, at expense of iron and sulfur released by destabilization of pyrite and other minerals in fault zone. Cartoons are modified after Patten et al. (2016).

hydrothermal vents is ~407°C (Haase et al., 2007). Therefore, postseismic hydrothermal fluid is highly unlikely to have induced the very localized alteration of pyrite in the fault zones investigated here.

This interpretation is supported by the SEM/EDS observations. Different textures of iron sulfides in the fault zone sediments unveil clues about their formation. In rims around framboidal pyrite, pyrrhotite occurs intergrown with barite (Figures 6e and 6f), which is a diagnostic mineral for hydrothermal processes (e.g., Rye, 2005). It strongly suggests that pyrrhotite has locally replaced pyrite as a result of thermal alteration. Similar neoformed pyrrhotite has also been described by Chou, Song, Aubourg, Song et al. (2012), who reported pyrrhotite reaction rims around pyrite grains in rocks from the Chelungpu fault zone, which accommodated the 1999 Mw 7.9 Chi-Chi earthquake. The halo textures around framboidal pyrite (Figure 6f) seem to be diagnostic of the presence of a hydrothermal fluid (induced by coseismic frictional heating); these halos delineate the limits of possible fluid migration with the associated pyrrhotite. Similar halo textures were also observed by Weaver et al. (2002) in an early Miocene mudstone sequence in the Okhta River section, Sakhalin (Russia), which was interpreted to have been altered by a tectonically driven fluid migration event. Such alteration is particularly apparent in Figures 6h and 6i, where pyrrhotite nucleated on a feldspar surface to form lath-like crystals. The morphology of the feldspar crystal appears to control the nodule shape and the distribution of pyrrhotite. Transient hydrothermal fluid is also likely to be associated with the formation of the pyrrhotite nodules surrounding silicates along fractures (Figures 6j and 6k), which act as conduits for migration of these coseismic hydrothermal fluids. Possibly, sulfide gradients in the fluid flow have resulted in different iron sulfide products (i.e., pyrite or pyrrhotite; e.g., Figure 6k).

5.3. Alteration of Pyrite to Pyrrhotite as Record of Seismic Slip

It is noteworthy that the thermomagnetic behavior of the present pyrrhotite resembles that of hydrothermally synthesized pyrrhotite, which was quenched from ~200°C to room temperature in <30 s, that is, comparable to seismic frictional heating processes (O'Reilly et al., 2000). It also resembles the behavior of pyrrhotite in hydrothermally altered sediments (Urbat et al., 2000). Such pyrrhotite is altering on heating in air during the high-temperature measurements (Figures 3j and 3k and S1l and S1m), in contrast to other pyrrhotites, which are thermally more stable with respect to heating in air (Urbat et al., 2000).

In addition, an anomalous concentration of H_2 is observed at ~697.4 m bsf (i.e., close to the fault zone FZ697) (Chester, Mori, et al., 2013). It is thought to have been produced by coseismic mechanochemical reactions during the earthquake, and to be a signature of earthquake events (e.g., Chester, Mori, et al., 2013; Hirose et al., 2011). Pyrite is thermodynamically unstable with respect to pyrrhotite in the presence of H_2, which would facilitate its decomposition (Lambert et al., 1998). This provides further compelling support for an earthquake-related origin of the pyrrhotite in these fault zones.

The pyrite-pyrrhotite reaction leads to an increase of magnetic susceptibility and magnetization (i.e., M_s and M_{rs}) within the fault zones (Figure 2). The neoformed pyrrhotite, which results from thermal decomposition of pyrite and/or precipitation of coseismic hot fluids, would carry either a thermochemical or even a thermoremanent magnetization. Also, the cooling of the slip zone would imprint a thermoremanent magnetization in the fault zone samples (Appel et al., 2012; Chou, Song, Aubourg, Lee et al., 2012). It is the most likely reason for the high NRM observed within the fault zones (Figure 2a). As mentioned earlier on the sample at 770.44 m bsf with a high NRM (Figure 2a and Table S1) without a visible slip zone, could well be a volcanic ash because of the abundant PSD magnetite in that sample (see Figure S1 in the supporting information).

The thermal decomposition/alteration of pyrite due to the seismic frictional heating and consequent coseismic hydrothermal fluid during an earthquake is summarized in Figure 8. With the temperature rise induced by the frictional heating, preexisting framboidal pyrite (Figure 8a) in the fault zone starts to decompose to pyrrhotite, and this reaction will accelerate when the temperature is over ~640°C. A pyrrhotite rim is then formed surrounding the pyrite core in case the reaction is incomplete (Figure 8b). Meanwhile, pyrite within the fault zone is leached by hot fluids derived from heating of sediment pore fluids, resulting in an altered rim consisting of intergrowths of pyrrhotite and barite (Figure 8c). These hydrothermal fluids percolated and infiltrated the fractures close to the slip zone, where destabilization of pyrite would release Fe that readily enters the fluid and is subsequently transported along the fractures. With cooling of these hot fluids, pyrite/pyrrhotite precipitated around the silicates present and/or pyrrhotite nucleated on feldspar grains (Figure 8d), as evidenced by SEM observations (Figures 6j and 6k). The newly formed pyrrhotite in a seismic slip zone is thus a robust indicator of past earthquake slip.

6. Conclusions

Integrated mineral magnetic measurements and SEM/EDS observations demonstrate the presence of pyrrhotite confined to three fault zones developed in deep-sea sediments cored from the Japan Trench, one of the seismically most active regions around Japan. The pyrrhotite originates from alteration of pyrite at high temperatures resulting from seismic frictional heating during earthquake slip. Next to a temperature rise coseismic hot fluids are produced within the fault zones. So in this setting the pyrrhotite should be considered a seismically induced mineral. Our rock magnetic and kinetic chemical modeling results indicate that occurrence of pyrrhotite in seismic fault zones appears to be intimately associated with earthquake slip events, and the peak temperature experienced by these slip zones is constrained to a range of 640–800°C. The rock magnetic identification of pyrrhotite is therefore very useful for assessing ancient earthquake events in pyrite-bearing sedimentary sequences. The frictional heat with its associated temperature rise can be constrained by examining the magnetic assemblages within a fault zone.

Acknowledgments
The core samples used in this study were provided by the IODP. We thank the drilling staff and laboratory technicians onboard the D/V *Chikyu* during the Expedition 343. T. Y.'s participation to the IODP Expedition 343 was supported by IODP-China. This research was supported by National Natural Science Foundation of China (NSFC) grants 41472177 and 41204062 and the Scientific Research Foundation for the Returned Overseas Chinese Scholars, Ministry of Human Resources and Social Security of the People's Republic of China (MOHRSS). Special thanks to Weiren Lin and Tsuyoshi Ishikawa for generously sharing part of the fault zone samples. We would like to thank Zhijian Niu for his assistance with the SEM/EDS observations. We also thank reviewer Mike Jackson and an anonymous reviewer, the Associate Editor, and the Editor Michael Walter for their comments that helped to improve the manuscript. T. Y. acknowledges the China Scholarship Council (CSC) for a visiting scholarship to Utrecht University (Netherlands). All data for this study are available from the corresponding author via e-mail: yangtao@cug.edu.cn, or t.yang@uu.nl.

References

Aben, F. M., Dekkers, M. J., Bakker, R. R., Hinsbergen, D. J. J., Zachariase, W. J., Tate, G. W., et al. (2014). Untangling inconsistent magnetic polarity records through an integrated rock magnetic analysis: A case study on Neogene sections in East Timor. *Geochemistry, Geophysics, Geosystems*, *15*, 2531–2554. https://doi.org/10.1002/2014GC005294

Abubakar, R., Muxworthy, A. R., Sephton, M. A., Southern, P., Watson, J. S., Fraser, A. J., & Almeida, T. P. (2015). Formation of magnetic minerals at hydrocarbon-generation conditions. *Marine and Petroleum Geology*, *68*, 509–519. https://doi.org/10.1016/j.marpetgeo.2015.10.003

Appel, E., Crouzet, C., & Schill, E. (2012). Pyrrhotite remagnetizations in the Himalaya: A review. *Geological Society of London, Special Publication*, *371*(1), 163–180. https://doi.org/10.1144/SP371.1

Argus, D. F., Gordon, R. G., & DeMets, C. (2011). Geologically current motion of 56 plates relative to the no-net-rotation reference frame. *Geochemistry, Geophysics, Geosystems*, *12*, Q11001. https://doi.org/10.1029/2011GC003751

Bayer, G. (1973). Thermal expansion anisotropy of oxide compounds. *Proceedings of the British Ceramic Society*, *22*, 39–53.

Bhargava, S. K., Garg, A., & Subasinghe, N. D. (2009). In situ high-temperature phase transformation studies on pyrite. *Fuel*, *88*(6), 988–993. https://doi.org/10.1016/j.fuel.2008.12.005

Brantut, N., Han, R., Shimamoto, T., Findling, N., & Schubnel, A. (2011). Fast slip with inhibited temperature rise due to mineral dehydration: Evidence from experiments on gypsum. *Geology*, *39*(1), 59–62. https://doi.org/10.1130/G31424.1

Brune, J. N., Henyey, T. L., & Roy, R. F. (1969). Heat flow, stress, and rate of slip along the San Andreas Fault, California. *Journal of Geophysical Research*, *74*(15), 3821–3827. https://doi.org/10.1029/JB074i015p03821

Center for Deep Earth Exploration (CDEX) (2012). Drilling program IODP Expedition 343: Japan Trench Fast Earthquake Drilling Project (JFAST), (CDEX Technical Report 16, pp. 1–99). Kanagawa, Japan: The Center for Deep Earth Exploration, Japan Agency for Marine-Earth Science and Technology.

Chen, J., Niemeijer, A., Yao, L., & Ma, S. (2017). Water vaporization promotes coseismic fluid pressurization and buffers temperature rise. *Geophysical Research Letters*, *44*, 2177–2185. https://doi.org/10.1002/2016GL071932

Chen, J., Niemeijer, A. R., & Fokker, P. A. (2017). Vaporization of fault water during seismic slip. *Journal of Geophysical Research: Solid Earth*, *122*, 4237–4276. https://doi.org/10.1002/2016JB013824

Chen, J., Yang, X., Duan, Q., Shimamoto, T., & Spiers, C. J. (2013). Importance of thermochemical pressurization in the dynamic weakening of the Longmenshan Fault during the 2008 Wenchuan earthquake: Inferences from experiments and modeling. *Journal of Geophysical Research: Solid Earth*, *118*, 4145–4169. https://doi.org/10.1002/jgrb.50260

Chen, J., Yang, X., Ma, S., Yang, T., & Niemeijer, A. (2016). Hydraulic properties of samples retrieved from the Wenchuan earthquake Fault Scientific Drilling Project Hole-1 (WFSD-1) and the surface rupture zone: Implications for coseismic slip weakening and fault healing. *Geochemistry, Geophysics, Geosystems*, *17*, 2717–2744. https://doi.org/10.1002/2016GC006376

Chester, F. M., Mori, J. J., Eguchi, N., Toczko, S., & Expedition 343/343T Scientists (2013). Proceedings of the Integrated Ocean Drilling Program. (Vol. 343/343T). Tokyo, Japan: Integrated Ocean Drilling Program Management International, Inc. https://doi.org/10.2204/iodp.proc.343343T.2013

Chester, F. M., Rowe, C., Ujiie, K., Kirkpatrick, J., Regalla, C., Remitti, F., et al. (2013). Structure and composition of the plate-boundary slip zone for the 2011 Tohoku-Oki earthquake. *Science*, *342*(6163), 1208–1211. https://doi.org/10.1126/science.1243719

Chou, Y.-M., Song, S.-R., Aubourg, C., Lee, T.-Q., Boullier, A.-M., Song, Y.-F., et al. (2012). An earthquake slip zone is a magnetic recorder. *Geology*, *40*(6), 551–554. https://doi.org/10.1130/G32864.1

Chou, Y.-M., Song, S.-R., Aubourg, C., Song, Y.-F., Boullier, A.-M., Lee, T.-Q., et al. (2012). Pyrite alteration and neoformed magnetic minerals in the fault zone of the Chi-Chi earthquake (Mw 7.6, 1999): Evidence for frictional heating and co-seismic fluids. *Geochemistry, Geophysics, Geosystems*, *13*, Q08002. https://doi.org/10.1029/2012GC004120

Cowan, D. S. (1999). Do faults preserve a record of seismic slip? A field geologist's opinion. *Journal of Structural Geology*, *21*(8-9), 995–1001. https://doi.org/10.1016/S0191-8141(99)00046-2

Craig, J. R., & Vokes, F. M. (1993). The metamorphism of pyrite and pyritic ores: An overview. *Mineralogical Magazine*, *57*(386), 3–18. https://doi.org/10.1180/minmag.1993.057.386.02

Day, R., Fuller, M., & Schmidt, V. A. (1977). Hysteresis properties of titanomagnetites: Grain-size and compositional dependence. *Physics of the Earth and Planetary Interiors*, *13*(4), 260–267. https://doi.org/10.1016/0031-9201(77)90108-X

Dekkers, M. J. (1988). Magnetic properties of natural pyrrhotite. Part I: Behaviour of initial susceptibility and saturation-magnetization-related rock-magnetic parameters in a grain-size dependent framework. *Physics of the Earth and Planetary Interiors*, *52*(3-4), 376–393. https://doi.org/10.1016/0031-9201(88)90129-X

Dekkers, M. J., Mattéi, J. L., Fillion, G., & Rochette, P. (1989). Grain-size dependence of the magnetic behavior of pyrrhotite during its low-temperature transition at 34 K. *Geophysical Research Letters*, *16*(8), 855–858. https://doi.org/10.1029/GL016i008p00855

Dekkers, M. J., Passier, H. F., & Schoonen, M. A. A. (2000). Magnetic properties of hydrothermally synthesised greigite (Fe_3S_4)—II. High- and low-temperature characteristics. *Geophysical Journal International*, *141*(3), 809–819. https://doi.org/10.1046/j.1365-246x.2000.00129.x

Dunlop, D. J., & Özdemir, Ö. (1997). *Rock Magnetism: Fundamentals and Frontiers*. Cambridge, UK: Cambridge University Press. https://doi.org/10.1017/CBO9780511612794

Fine, R. A., & Millero, F. J. (1973). Compressibility of water as a function of temperature and pressure. *The Journal of Chemical Physics*, *59*(10), 5529–5536. https://doi.org/10.1063/1.1679903

Fulton, P. M., Brodsky, E. E., Kano, Y., Mori, J., Chester, F., Ishikawa, T., et al. (2013). Low coseismic friction on the Tohoku-Oki fault determined from temperature measurements. *Science*, *342*(6163), 1214–1217. https://doi.org/10.1126/science.1243641

Gillett, S. L. (2003). Paleomagnetism of the Notch Peak contact metamorphic aureole, revisited: Pyrrhotite from magnetite+pyrite under submetamorphic conditions. *Journal of Geophysical Research*, *108*(B9), 2446. https://doi.org/10.1029/2002JB002386

Haase, K. M., Petersen, S., Koschinsky, A., Seifert, R., Devey, C. W., Keir, R., et al. (2007). Young volcanism and related hydrothermal activity at 5°S on the slow-spreading southern Mid-Atlantic Ridge. *Geochemistry, Geophysics, Geosystems*, *8*, Q11002. https://doi.org/10.1029/2006GC001509

Han, R., Shimamoto, T., Ando, J.-I., & Ree, J.-H. (2007). Seismic slip record in carbonate-bearing fault zones: An insight from high-velocity friction experiments on siderite gouge. *Geology*, *35*(12), 1131–1134. https://doi.org/10.1130/G24106A.1

Harrison, R. J., & Feinberg, J. M. (2008). FORCinel: An improved algorithm for calculating first-order reversal curve distributions using locally weighted regression smoothing. *Geochemistry, Geophysics, Geosystems*, *9*, Q05016. https://doi.org/10.1029/2008GC001987

Hirose, T., & Bystricky, M. (2007). Extreme dynamic weakening of faults during dehydration by coseismic shear heating. *Geophysical Research Letters*, *34*, L14311. https://doi.org/10.1029/2007GL030049

Hirose, T., Kawagucci, S., & Suzuki, K. (2011). Mechanoradical H_2 generation during simulated faulting: Implications for an earthquake-driven subsurface biosphere. *Geophysical Research Letters*, *38*, L17303. https://doi.org/10.1029/2011GL048850

Hoare, I. C., & Levy, J. H. (1990). The non-isothermal reaction kinetics of pyrite with water vapor. *Thermochimica Acta*, *164*, 153–160. https://doi.org/10.1016/0040-6031(90)80432-X

Housen, B. A., & Musgrave, R. J. (1996). Rock-magnetic signature of gas hydrates in accretionary prism sediments. *Earth and Planetary Science Letters*, *139*(3-4), 509–519. https://doi.org/10.1016/0012-821X(95)00245-8

Hu, G., Dam-Johansen, K., Wedel, S., & Hansen, J. P. (2006). Decomposition and oxidation of pyrite. *Progress in Energy and Combustion Science*, *32*(3), 295–314. https://doi.org/10.1016/j.pecs.2005.11.004

Hyndman, R. D., & Spence, G. D. (1992). A seismic study of methane hydrate marine bottom simulating reflectors. *Journal of Geophysical Research*, *97*(B5), 6683–6698. https://doi.org/10.1029/92JB00234

Ishikawa, T., Tanimizu, M., Nagaishi, K., Matsuoka, J., Tadai, O., Sakaguchi, M., et al. (2008). Coseismic fluid-rock interactions at high temperatures in the Chelungpu fault. *Nature Geoscience*, *1*(10), 679–683. https://doi.org/10.1038/ngeo308

Kanamori, H., Miyazawa, M., & Mori, J. (2006). Investigation of the earthquake sequence off Miyagi prefecture with historical seismograms. *Earth, Planets and Space*, *58*(12), 1533–1541. https://doi.org/10.1186/bf03352657

Kano, Y., Mori, J., Fujio, R., Ito, H., Yanagidani, T., Nakao, S., & Ma, K.-F. (2006). Heat signature on the Chelungpu fault associated with the 1999 Chi-Chi, Taiwan earthquake. *Geophysical Research Letters*, *33*, L14306. https://doi.org/10.1029/2006GL026733

Kars, M., & Kodama, K. (2015). Authigenesis of magnetic minerals in gas hydrate-bearing sediments in the Nankai Trough, offshore Japan. *Geochemistry, Geophysics, Geosystems*, *16*, 947–961. https://doi.org/10.1002/2014GC005614

Keren, T. T., & Kirkpatrick, J. D. (2016). The damage is done: Low fault friction recorded in the damage zone of the shallow Japan Trench décollement. *Journal of Geophysical Research: Solid Earth*, *121*, 3804–3824. https://doi.org/10.1002/2015JB012311

Kirkpatrick, J. D., Rowe, C. D., Ujiie, K., Moore, J. C., Regalla, C., Remitti, F., et al. (2015). Structure and lithology of the Japan Trench subduction plate boundary fault. *Tectonics*, *34*, 53–69. https://doi.org/10.1002/2014TC003695

Kuo, L.-W., Di Felice, F., Spagnuolo, E., Di Toro, G., Song, S.-R., Aretusini, S., et al. (2017). Fault gouge graphitization as evidence of past seismic slip. *Geology*, *45*(11), 979–982. https://doi.org/10.1130/G39295.1

Kuo, L.-W., Song, S.-R., Suppe, J., & Yeh, E.-C. (2016). Fault mirrors in seismically active fault zones: A fossil of small earthquakes at shallow depths. *Geophysical Research Letters*, *43*, 1950–1959. https://doi.org/10.1002/2015GL066882

Lachenbruch, A. H., & Sass, J. H. (1980). Heat-flow and energetics of the San-Andreas fault zone. *Journal of Geophysical Research*, *85*(B11), 6185–6222. https://doi.org/10.1029/JB085iB11p06185

Lambert, J. M. Jr., Simkovich, G., & Walker, P. L. Jr. (1998). The kinetics and mechanism of the pyrite-to-pyrrhotite transformation. *Metallurgical and Materials Transactions B*, *29*(2), 385–396. https://doi.org/10.1007/s11663-998-0115-x

Larrasoaña, J. C., Roberts, A. P., Musgrave, R. J., Gràcia, E., Piñero, E., Vega, M., & Martinez-Ruiz, F. (2007). Diagenetic formation of greigite and pyrrhotite in gas hydrate marine sedimentary systems. *Earth and Planetary Science Letters*, *261*(3-4), 350–366. https://doi.org/10.1016/j.epsl.2007.06.032

Lay, T., & Bilek, S. (2007). Anomalous earthquake ruptures at shallow depths on subduction zone megathrusts. In T. H. Dixon & J. C. Moore (Eds.), *The Seismogenic Zone of Subduction Thrust Faults* (pp. 476–511). New York: Columbia University Press. https://doi.org/10.7312/dixo13866-015

Li, H., Xue, L., Brodsky, E. E., Mori, J. J., Fulton, P. M., Wang, H., et al. (2015). Long-term temperature records following the Mw 7.9 Wenchuan (China) earthquake consistent with low friction. *Geology*, *43*(2), 163–166. https://doi.org/10.1130/G35515.1

Li, H.-Y., & Zhang, S.-H. (2005). Detection of mineralogical changes in pyrite using measurements of temperature-dependence susceptibilities. *Chinese Journal of Geophysics*, *48*(6), 1454–1461. https://doi.org/10.1002/cjg2.794

Lin, A. (2008). *Fossil Earthquakes: The Formation and Preservation of Pseudotachylytes*. Berlin, Germany: Springer.

Lin, W., Fulton, P. M., Harris, R. N., Tadai, O., Matsubayashi, O., Tanikawa, W., & Kinoshita, M. (2014). Thermal conductivities, thermal diffusivities, and volumetric heat capacities of core samples obtained from the Japan Trench Fast Drilling Project (JFAST). *Earth, Planets and Space*, *66*(1), 48. https://doi.org/10.1186/1880-5981-66-48

Machel, H. G. (2001). Bacterial and thermochemical sulfate reduction in diagenetic settings—Old and new insights. *Sedimentary Geology*, *140*(1-2), 143–175. https://doi.org/10.1016/S0037-0738(00)00176-7

Manning, E. B., & Elmore, R. D. (2015). An integrated paleomagnetic, rock magnetic, and geochemical study of the Marcellus shale in the Valley and Ridge province in Pennsylvania and West Virginia. *Journal of Geophysical Research: Solid Earth*, *120*, 705–724. https://doi.org/10.1002/2014JB011418

Mullender, T. A. T., van Velzen, A. J., & Dekkers, M. J. (1993). Continuous drift correction and separate identification of ferrimagnetic and paramagnetic contribution in thermomagnetic runs. *Geophysical Journal International*, *114*(3), 663–672. https://doi.org/10.1111/j.1365-246X.1993.tb06995.x

Muxworthy, A. R., & McClelland, E. (2000). Review of the low-temperature magnetic properties of magnetite from a rock magnetic perspective. *Geophysical Journal International*, *140*(1), 101–114. https://doi.org/10.1046/j.1365-246x.2000.00999.x

Oohashi, K., Hirose, T., & Shimamoto, T. (2011). Shear-induced graphitization of carbonaceous materials during seismic fault motion: Experiments and possible implications fault mechanics. *Journal of Structural Geology*, *33*(6), 1122–1134. https://doi.org/10.1016/j.jsg.2011.01.007

O'Reilly, W., Hoffmann, V., Chouker, A. C., Soffel, H. C., & Menyer, A. (2000). Magnetic properties of synthetic analogues of pyrrhotite ore in the grain size range 1–24 μm. *Geophysical Journal International*, *142*(3), 669–683. https://doi.org/10.1046/j.1365-246x.2000.00169.x

Özdemir, Ö., Dunlop, D., & Moskowitz, B. (2002). Changes in remanence, coercivity and domain state at low-temperature in magnetite. *Earth and Planetary Science Letters*, *194*(3-4), 343–358. https://doi.org/10.1016/S0012-821X(01)00562-3

Patten, C. G. C., Pitcairn, I. K., Teagle, D. A. H., & Harris, M. (2016). Sulphide mineral evolution and metal mobility during alteration of the oceanic crust: Insights from ODP Hole 1256D. *Geochimica et Cosmochimica Acta*, *193*, 132–159. https://doi.org/10.1016/j.gca.2016.08.009

Peters, C., & Dekkers, M. J. (2003). Selected room temperature magnetic parameters as a function of mineralogy, concentration and grain size. *Physics and Chemistry of the Earth*, *28*(16-19), 659–667. https://doi.org/10.1016/S1474-7065(03)00120-7

Peters, C., & Thompson, R. (1998). Magnetic identification of selected natural iron oxides and sulphides. *Journal of Magnetism and Magnetic Materials*, *183*(3), 365–374. https://doi.org/10.1016/S0304-8853(97)01097-4

Pike, C. R., Roberts, A. P., & Verosub, K. L. (1999). Characterizing interactions in fine magnetic particle systems using first order reversal curves. *Journal of Applied Physics*, *85*(9), 6660–6667. https://doi.org/10.1063/1.370176

Rabinowitz, H. S., Polissar, P. J., & Savage, H. M. (2017). Reaction kinetics of alkenone and *n*-alkane thermal alteration at seismic timescales. *Geochemistry, Geophysics, Geosystems*, *18*, 204–219. https://doi.org/10.1002/2016GC006553

Rabinowitz, H. S., Savage, H. M., Plank, T., Polissar, P. J., Kirkpatrick, J. D., & Rowe, C. D. (2015). Multiple major faults at the Japan Trench: Chemostratigraphy of the plate boundary at IODP Exp. 343: JFAST. *Earth and Planetary Science Letters*, *423*, 57–66. https://doi.org/10.1016/j.epsl.2015.04.010

Rabinowitz, H. S., Savage, H. M., Polissar, P. J., Plank, T. A., Rowe, C. D., & Kirkpatrick, J. D. (2013). Detecting the frictional temperature rise during the 2011 Tohoku Earthquake using the thermal maturity of biomarkers. Abstract T41F-07 Presented at the 2013 AGU Fall Meeting, San Francisco, CA.

Rice, J. R. (2006). Heating and weakening of faults during earthquake slip. *Journal of Geophysical Research*, *111*, B05311. https://doi.org/10.1029/2005JB004006

Roberts, A. P., Almeida, T. P., Church, N. S., Harrison, R. J., Heslop, D., Li, Y., et al. (2017). Resolving the origin of pseudo-single domain magnetic behavior. *Journal of Geophysical Research: Solid Earth*, *122*, 9534–9558. https://doi.org/10.1002/2017JB014860

Roberts, A. P., Chang, L., Rowan, C. J., Horng, C.-S., & Florindo, F. (2011). Magnetic properties of sedimentary greigite (Fe_3S_4): An update. *Reviews of Geophysics*, *49*, RG1002. https://doi.org/10.1029/2010RG000336

Roberts, A. P., Heslop, D., Zhao, X., & Pike, C. R. (2014). Understanding fine magnetic particle systems through use of first-order reversal curve diagrams. *Reviews of Geophysics*, *52*, 557–602. https://doi.org/10.1002/2014RG000462

Roberts, A. P., Pike, C. R., & Verosub, K. L. (2000). First-order reversal curve diagrams: A new tool for characterizing the magnetic properties of natural samples. *Journal of Geophysical Research*, *105*(B12), 28,461–28,475. https://doi.org/10.1029/2000JB900326

Roberts, A. P., & Weaver, R. (2005). Multiple mechanisms of remagnetization involving sedimentary greigite (Fe_3S_4). *Earth and Planetary Science Letters*, *231*(3-4), 263–277. https://doi.org/10.1016/j.epsl.2004.11.024

Rochette, P., Fillion, G., Mattéi, J.-L., & Dekkers, M. J. (1990). Magnetic transition at 30–34 Kelvin in pyrrhotite: Insight into a widespread occurrence of this mineral in rocks. *Earth and Planetary Science Letters*, *98*(3-4), 319–328. https://doi.org/10.1016/0012-821X(90)90034-U

Rowe, C. D., Fagereng, Å., Miller, J. A., & Mapani, B. (2012). Signature of coseismic decarbonation in dolomite fault rocks of the Naukluft Thrust, Namibia. *Earth and Planetary Science Letters*, *333–334*, 200–210.

Rowe, C. D., & Griffith, W. A. (2015). Do faults preserve a record of seismic slip: A second opinion. *Journal of Structural Geology*, *78*, 1–26. https://doi.org/10.1016/j.jsg.2015.06.006

Rye, R. O. (2005). A review of the stable-isotope geochemistry of sulfate minerals in selected igneous environments and related hydrothermal systems. *Chemical Geology*, *215*(1-4), 5–36. https://doi.org/10.1016/j.chemgeo.2004.06.034

Savage, H. M., Polissar, P. J., Sheppard, R., Rowe, C. D., & Brodsky, E. E. (2014). Biomarkers heat up during earthquakes: New evidence of seismic slip in the rock record. *Geology*, *42*(2), 99–102. https://doi.org/10.1130/G34901.1

Sawai, Y., Namegaya, Y., Tamura, T., Nakashima, R., & Tanigawa, K. (2015). Shorter intervals between great earthquakes near Sendai: Scour ponds and a sand layer attributable to A.D. 1454 overwash. *Geophysical Research Letters*, *42*, 4795–4800. https://doi.org/10.1002/2015GL064167

Scholz, C. H. (2002). *The Mechanisms of Earthquake Faulting*. Cambridge: Cambridge University Press. https://doi.org/10.1017/CBO9780511818516

Scholz, C. H. (2014). The rupture mode of the shallow large-slip surge of the Tohoku-oki earthquake. *Bulletin of the Seismological Society of America*, *104*(5), 2627–2631. https://doi.org/10.1785/0120140130

Sibson, R. H. (2003). Thickness of the seismic slip zone. *Bulletin of the Seismological Society of America*, *93*(3), 1169–1178. https://doi.org/10.1785/0120020061

Sibson, R. H., & Toy, V. G. (2006). The habitat of fault-generated pseudotachylyte: Presence vs. absence of friction-melt. In R. Abercrombie, A. McGarr, H. Kanamori, & G. Di Toro (Eds.), *Earthquakes: Radiated Energy and the Physics of Faulting, Geophysical Monograph Series* (Vol. 170, pp. 153–166). Washington, DC: American Geophysical Union.

Simons, M., Minson, S. E., Sladen, A., Ortega, F., Jiang, J., Owen, S. E., et al. (2011). The 2011 magnitude 9.0 Tohoku-Oki earthquake: Mosaicking the megathrust from seconds to centuries. *Science*, *332*(6036), 1421–1425. https://doi.org/10.1126/science.1206731

Sulem, J., & Famin, V. (2009). Thermal decomposition of carbonates in fault zones: Slip-weakening and temperature-limiting effects. *Journal of Geophysical Research*, *114*, B03309. https://doi.org/10.1029/2008JB006004

Sutherland, R., Townend, J., Toy, V., Upton, P., Coussens, J., Allen, M., et al. (2017). Extreme hydrothermal conditions at an active plate-bounding fault. *Nature*, *546*(7656), 137–140. https://doi.org/10.1038/nature22355

Swanson, M. T. (1992). Fault structure, wear mechanisms and rupture processes in pseudotachylyte generation. *Tectonophysics*, *204*(3-4), 223–242. https://doi.org/10.1016/0040-1951(92)90309-T

Tanikawa, W., Hirose, T., Mukoyoshi, H., Tadai, O., & Lin, W. (2013). Fluid transport properties in sediments and their role in large slip near the surface of the plate boundary fault in the Japan Trench. *Earth and Planetary Science Letters*, *382*, 150–160. https://doi.org/10.1016/j.epsl.2013.08.052

Tanikawa, W., Ishikawa, T., Honda, G., Hirono, T., & Tadai, O. (2015). Trace element anomaly in fault rock induced by coseismic hydrothermal reactions reproduced in laboratory friction experiments. *Geophysical Research Letters*, *42*, 3210–3217. https://doi.org/10.1002/2015GL063195

Togo, T., Shimamoto, T., Ma, S., Wen, X., & He, H. (2011). Internal structure of Longmenshan fault zone at Hongkou outcrop, Sichuan, China, that caused the 2008 Wenchuan earthquake. *Earthquake Science*, *24*(3), 249–265. https://doi.org/10.1007/s11589-011-0789-z

Torii, M., Fukuma, K., Horng, C.-S., & Lee, T.-Q. (1996). Magnetic discrimination of pyrrhotite- and greigite-bearing sediment samples. *Geophysical Research Letters*, *23*(14), 1813–1816. https://doi.org/10.1029/96GL01626

Ujiie, K., Inoue, T., & Ishiwata, J. (2016). High-velocity frictional strength across the Tohoku-Oki megathrust determined from surface drilling torque. *Geophysical Research Letters*, *43*, 2488–2493. https://doi.org/10.1002/2016GL067671

Urbat, M., Dekkers, M. J., & Krumsiek, K. (2000). Discharge of hydrothermal fluids through sediment at the Escanaba Trough, Gorda Ridge (ODP Leg 169): Assessing the effects on the rock magnetic signal. *Earth and Planetary Science Letters*, *176*(3-4), 481–494. https://doi.org/10.1016/S0012-821X(00)00024-8

Volk, M. W. R., Gilder, S. A., & Feinberg, J. M. (2016). Low-temperature magnetic properties of monoclinic pyrrhotite with particular relevance to the Besnus transition. *Geophysical Journal International*, *207*(3), 1783–1795. https://doi.org/10.1093/gji/ggw376

Weaver, R., Roberts, A. P., & Barker, A. J. (2002). A late diagenetic (syn-folding) magnetization carried by pyrrhotite: Implications for paleomagnetic studies from magnetic iron sulphide-bearing sediments. *Earth and Planetary Science Letters*, *200*(3-4), 371–386. https://doi.org/10.1016/S0012-821X(02)00652-0

Wehland, F., Stancu, A., Rochette, P., Dekkers, M. J., & Appel, E. (2005). Experimental evaluation of magnetic interaction in pyrrhotitebearing samples. *Physics of the Earth and Planetary Interiors*, *153*(4), 181–190. https://doi.org/10.1016/j.pepi.2005.05.006

Yang, T., Dekkers, M. J., & Zhang, B. (2016). Seismic heating signatures in the Japan Trench subduction plate-boundary fault zone: Evidence from a preliminary rock magnetic 'geothermometer'. *Geophysical Journal International*, *205*(1), 332–344.

Yue, H., & Lay, T. (2011). Inversion of high-rate (1 sps) GPS data for rupture process of the 11 March 2011 Tohoku earthquake (Mw 9.1). *Geophysical Research Letters*, *38*, L00G09. https://doi.org/10.1029/2011GL048700

Zheng, G.-D., Lang, Y.-H., Takano, B., Matsuo, M., Kuno, A., & Tsushima, H. (2002). Iron speciation of sliding mud in Toyama prefecture, Japan. *Journal of Asian Earth Sciences*, *20*(8), 955–963. https://doi.org/10.1016/S1367-9120(01)00088-8